PNAS RESEARCH ARTICLE | EARTH, ATMOSPHERIC, AND PLANETARY SCIENCES OPEN ACCESS

4D microvelocimetry reveals multiphase flow field perturbations in porous media

Tom Bultreys[a,b,1], Sharon Ellman[a,b], Christian M. Schlepütz[c], Matthieu N. Boone[a,d], Gülce Kalyoncu Pakkaner[a,b], Shan Wang[a,b], Mostafa Borji[a,b], Stefanie Van Offenwert[a,b], Niloofar Moazami Goudarzi[a,d], Wannes Goethals[a,d], Chandra Widyananda Winardhi[a,b], and Veerle Cnudde[a,b,e]

Edited by David Weitz, Harvard University, Cambridge, MA; received September 26, 2023; accepted February 4, 2024

Many environmental and industrial processes depend on how fluids displace each other in porous materials. However, the flow dynamics that govern this process are still poorly understood, hampered by the lack of methods to measure flows in optically opaque, microscopic geometries. We introduce a 4D microvelocimetry method based on high-resolution X-ray computed tomography with fast imaging rates (up to 4 Hz). We use this to measure flow fields during unsteady-state drainage, injecting a viscous fluid into rock and filter samples. This provides experimental insight into the nonequilibrium energy dynamics of this process. We show that fluid displacements convert surface energy into kinetic energy. The latter corresponds to velocity perturbations in the pore-scale flow field behind the invading fluid front, reaching local velocities more than 40 times faster than the constant pump rate. The characteristic length scale of these perturbations exceeds the characteristic pore size by more than an order of magnitude. These flow field observations suggest that nonlocal dynamic effects may be long-ranged even at low capillary numbers, impacting the local viscous-capillary force balance and the representative elementary volume. Furthermore, the velocity perturbations can enhance unsaturated dispersive mixing and colloid transport and yet, are not accounted for in current models. Overall, this work shows that 4D X-ray velocimetry opens the way to solve long-standing fundamental questions regarding flow and transport in porous materials, underlying models of, e.g., groundwater pollution remediation and subsurface storage of CO_2 and hydrogen.

multiphase flow | porous media | 3D velocimetry | hydrogeology

Many processes in nature and engineering depend on the simultaneous presence of multiple fluids inside a porous medium. Examples include air and water in soils during groundwater recharge, storage of hydrogen and carbon dioxide in brine-filled porous rock layers in the deep subsurface, and water–gas management in fuel cells. However, the standard macroscopic model for creeping fluid flows in these systems, Darcy's law extended to two-phase flow, breaks down at much lower flow rates than nondimensional analysis would suggest (1, 2). For example, it cannot explain nonmonotonic soil–water profiles (3, 4) and anomalous flow resistance at low flow rates (5–8). This can be traced back to oversimplification of how the microscopic fluid dynamics in the pores are represented (2, 9–12). This results in difficulties to predict how fluids displace each other and consequently how dissolved chemicals and colloids such as pollutants and microbial life are transported in porous materials not saturated by one single fluid (13, 14)—as is commonly the case.

The development of time-resolved X-ray micro-computed tomography (micro-CT) has made it possible to observe meniscus motions inside pore spaces in, e.g., geological materials (15–18). This has shown that menisci undergo complex, fluctuating dynamics even during slow flows expected to proceed in quasiequilibrium (19–23). The dynamics are due to the interplay between capillary forces, viscous friction, and inertia. Capillary forces cause instabilities which can trigger sudden meniscus rearrangements (e.g., Haines jumps and snap-off events) (16, 17, 22, 24–27). The associated flows in the two fluids are presumed to cause viscous and inertial contributions that affect the pressures across fluid menisci in neighboring pores, which can in turn trigger further rearrangement (28–30). In certain cases, this can even lead to oscillating ("intermittent") fluid occupancy in specific pores (20). However, key questions remain open: How do these single-pore events influence the flow at the network scale? What are the characteristic length, time, and energy scales involved? These questions are important for the development of models which propose a consistent upscaling of multiphase flow from the pore to the continuum scale, for example, based on energy fluctuation statistics in nonequilibrium statistical mechanics (31, 32). Furthermore, they are key to understanding whether there is an impact on solute and colloid transport during transient flows, including rain intrusion in dry soil (14, 33). To resolve these questions, the unsteady flow field throughout the pores must be studied.

Significance

Models of multiphase fluid flows in porous materials commonly struggle to capture the effects of the underlying microscopic dynamics. These flows are very common: Examples range from groundwater flow and H_2 storage in underground rocks to water discharge in fuel cells. The microscopic dynamics are poorly understood because they are so far inaccessible in nearly all 3D pore geometries, hampered by the optical opacity of the materials. Here, we introduce a method to measure unsteady 3D flow fields in opaque materials, based on synchrotron X-ray imaging. We observe strong perturbations in pore-scale velocity fields during drainage, with important implications for the energy dynamics and flow regimes of multiphase flow, and for dispersive mixing and colloid transport in unsaturated porous media.

Author contributions: T.B. designed research; T.B., S.E., C.M.S., M.N.B., G.K.P., S.W., M.B., S.V.O., N.M.G., W.G., and V.C. performed research; C.M.S. contributed new reagents/analytic tools; T.B., S.E., and C.W.W. analyzed data; T.B. project administration, funding acquisition and supervision; V.C. project supervision, funding acquisition; and T.B. wrote the original draft. All authors reviewed and edited the draft.

The authors declare no competing interest.

This article is a PNAS Direct Submission.

[1]To whom correspondence may be addressed. Email: Tom.Bultreys@UGent.be.

This article contains supporting information online at https://www.pnas.org/lookup/suppl/doi:10.1073/pnas.2316723121/-/DCSupplemental.

Published March 13, 2024.

A key difficulty is therefore the methodological challenge of measuring flow fields inside three-dimensional, microscopic pore networks of porous materials.

Here, we present direct measurements of unsteady 3D flow fields during pore-scale fluid displacements in porous materials. To capture these flows, a velocimetry method must be fast, fully three-dimensional and have a μm-scale resolution. Furthermore, it must probe spatially heterogeneous, tortuous velocity fields. The state-of-the-art in microvelocimetry has been based on optical measurements, e.g., in micromodels (34–36) and in a few recent cases in 3D glass beads packs (37–40). However, optical access requires transparent porous materials, fluid index matching, and sparse tracer seeding. Furthermore, simplified pore geometries may not replicate the full complexity of the dynamics (41–43). Ultrasound and MRI velocimetry work for opaque 3D materials but do not simultaneously reach the required spatial and temporal resolutions (44, 45). X-ray velocimetry is promising (46–51) but was until recently not applied to flows in porous media, mainly due to the challenge of reconstructing 3D flows in complex geometries. A recent approach to this is the use of time-resolved X-ray micro-CT to track tracer microparticles in the flow (52, 53). However, these works have dealt with steady, creeping flows in porous media due to limitations in the temporal resolution.

To overcome the current limitations on 3D X-ray velocimetry, we present unique experiments based on fast synchrotron micro-computed tomography (micro-CT) at the TOMCAT beamline of the Swiss Light Source synchrotron (SLS). Using this method, we track tracer particles in the pores of sintered glass filter and limestone samples (4 mm diameter, 10 mm long) during drainage, in order to sample the unsteady 3D three-component (3D3C) velocity vector field. With the resulting data, we characterize the flow field dynamics triggered by Haines jumps. We quantify the spatial and temporal characteristics of the perturbations, and perform detailed measurements of the associated nonequilibrium energy dynamics.

1. Results

1.1. Haines Jumps Trigger Capillary-Driven Flow Field Perturbations. Our experiments give unique insights into how time-dependent flow fields behave during capillary-dominated fluid displacements. Viscous silicone oil seeded with flow tracers (~10 μm diameter silver-coated hollow spheres) is injected into a brine-saturated sample at a slow constant pump rate, achieving capillary numbers $Ca \sim 10^{-6}$ ($Ca = \mu v/\sigma$, with μ the viscosity, v the characteristic flow rate, and σ the interfacial tension). The micro-CT imaging of this process spans a time window of 50 s with a time resolution of either 0.25 s or 0.50 s and an isotropic voxel size of 2.75 μm. In the resulting time series of 3D images, we track both the fluid menisci and the flow tracers. Experimental details are discussed in Section 3.

The dataset of the sintered glass experiment reveals the dynamics before, during, and after a Haines jump. A Haines jump is the process by which a fluid meniscus invades one or multiple pores in a sudden accelerated movement during drainage, despite the fact that the externally imposed flow rate is constant (54). This is known to be caused by the dominance of capillary forces: the nonwetting phase (here: oil) prefers to reside in larger pores, causing the meniscus to encounter an energetically unstable situation when it passes through a local constriction. In our experiment, we image Haines jump dynamics at an image acquisition rate of 4 Hz by combining the latest imaging improvements at the TOMCAT beamline with a setup that allows for continuous imaging while precisely controlling the flow. Contrary to previous micro-CT experiments on Haines jumps reported in the literature (16, 55–57), this is fast enough to capture the meniscus movement during the Haines jump, as well as the transient flow field in the oil.

- Acceleration of the advancing meniscus: At the moment defined as time zero (0 s), the oil meniscus suddenly accelerates forward into one of the pores (Fig. 1). After an acceleration phase of ~1 s, the meniscus locally reaches a maximum velocity of 163 μm/s (*SI Appendix*, *Materials* and Fig. S1). This is approximately 200 times faster than the interstitial flow rate (u_{pump} = 0.82 μm/s) estimated from the pump rate. The invasion proceeds sequentially through several pores. Note that the acceleration phase takes longer than the ms-time scale estimated in water–decane fluid systems (16) due to the high viscosity of the silicone oil.
- Retraction of surrounding menisci and capillary pressure decrease: The fast meniscus advancement during the Haines jump causes oil menisci in surrounding pores to retract, as the external oil supply delivered by the constant-rate pump cannot keep up (Fig. 1*A*). The deficit results in a rapid decrease in the (capillary) pressure difference between oil and brine, quantified here by the mean curvature of the fluid–fluid menisci in the image (Fig. 1*B*). It causes the volumetric rate of oil retraction in the sample to temporarily exceed the constant pump rate by a factor 10 (Fig. 1*C*). This confirms that previous observations of externally measured pressure perturbations during drainage (16, 27, 58) correspond to fluid redistribution caused by Haines jumps. We do not observe oscillating meniscus movements due to inertial forces (27), as these are dampened by the high viscosity of the oil.
- Transients in the flow field: The Haines jump causes a significant change to the flow field in the oil-filled pores (Fig. 2). The flow velocity increase starts at the location of the Haines jump and spreads throughout nearly the entire oil phase during the aforementioned acceleration phase. This reflects the redistribution of oil from the surrounding pores toward the Haines jump, by meniscus retraction in the former. The disturbance to the flow field is fairly long-lived: It dissipates over a time scale 30 times slower than the acceleration phase (30 s vs. 1 s), with smaller peaks reflecting the accelerations as several secondary pores are invaded.
- Fast, tortuous flow paths: During and after the acceleration phase, the flow field is remarkably tortuous and even undergoes significant flow reversal opposite to the injection direction (Fig. 2, as indicated on rendering number 4). Even before the Haines jump, the mean flow velocity of the tracers is higher than the interstitial flow rate (Fig. 2*A*) due to the tortuosity of the oil flow pathways. At its peak, the mean velocity is an order of magnitude higher than the interstitial flow rate, with locally even stronger excursions (Section 1.3).

The experiments therefore resulted in the following findings:

Image-based contact angles have a mean value of approximately 45°, varying slightly over time (*SI Appendix*, Fig. S2). While this mean value is in line with previous image-based measurements on glass beads (59), there is a large uncertainty on the measurement due to the rather basic threshold segmentation algorithm used here. Manual measurements on the 3D images yielded contact angles between 30° and 40° in the vicinity of the Haines jump.

Additional measurements on the Ketton limestone sample (*SI Appendix*, Figs. S3 and S4) confirm the observation of flow field perturbations that originate at Haines jumps and reach far

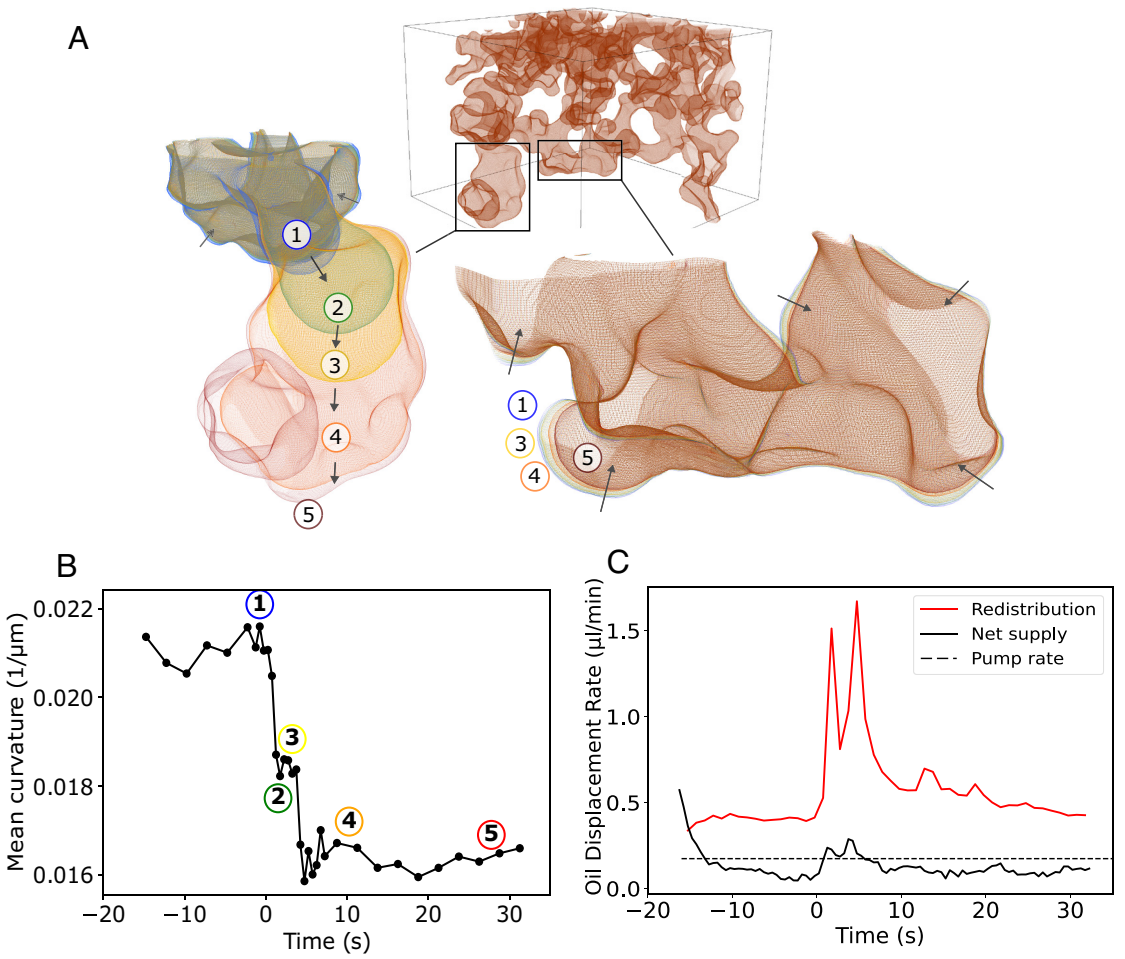

Fig. 1. The anatomy of a Haines jump in the porous filter sample; shown in (*A*) by rendering the fluid–fluid menisci. The *Inset* on the left highlights the fast-moving advancing fluid meniscus at five different time points. The local flow rate exceeds the external flow rate and therefore draws fluid in from the surrounding pores. This results in retracting fluid menisci highlighted for the same time points on the right. (*B*) The Haines jump is associated with a drop in the mean curvature of the fluid–fluid menisci, which has a one-to-one relation with the pressure difference between the fluids. The time points indicated here correspond to those in panel *A*. (*C*) The rate of internal oil redistribution during the Haines jump at time zero is higher than the net invasion rate supplied by the pump.

into the surrounding pore network. Here, the higher geometric complexity of the sample leads to more complex displacements: The retraction of neighboring fluid menisci during the Haines jump leads to entire pores refilling with brine and to temporary disconnection of the leading oil meniscus from the rest of the cluster ("Roof snap-off"). This complexity is mirrored in the flow field behavior, which has more temporal variability and a more intricate topology than in the filter sample.

1.2. Nonequilibrium Energy Dynamics Reflect Charging and Discharging of Surface Energy. Here, we show how velocimetry can be used to make the first steps toward experimentally quantifying energy perturbations during unsteady multiphase flows. Of key interest are the time scales of energy perturbations in the system, as this determines whether the system obeys a stationary energy balance needed to perform consistent upscaling (60) (no net input of energy into a particular region over a particular time scale). Energy conservation requires that the infinitesimal external work of the pump (dW_{pump}) must, at each moment in time, equal the sum of

- the pressure–volume work to change the fluid saturation in the pores (dW_{PV}),
- the change in surface energy stored in the fluid menisci (dE_s),
- the change in kinetic energy of the fluid flow (dE_{kin}),
- the dissipated heat ($d\Phi$).

$$\frac{dW_{pump}}{dt} = \frac{dW_{PV}}{dt} + \frac{dE_S}{dt} + \frac{dE_{kin}}{dt} + \frac{d\Phi}{dt}.$$

The combination of fluid distributions and velocimetry in our imaging data allows us to estimate the time evolution of these energy contributions (except the heat dissipation). Note that we do not have tracer particles in the brine phase, and hence we estimate the total kinetic energy in the system as twice that of the oil phase (given the similar mass densities and incompressibility). The surface energy calculation depends on the contact angle, which we set to 35° with a ±10° uncertainty bound. All the nonwetting fluid phase in the sample is in the field of view of the images (i.e. we imaged before oil breakthrough; the sample itself is larger than the field of view). Surface area estimates may be sensitive to image noise.

The Fig. 3 shows that the time window of the glass filter experiment can be divided into three phases. First, there is a "charging" phase, where the pressure–volume work performed by the pump is transferred into a near-equal increase in surface energy. The kinetic energy is small and remains nearly constant, indicating that most of the flow field resembles a steady Stokes flow. During this phase, the curvature of the menisci, and thus the capillary pressure, increases.

When the threshold for the Haines jump to proceed is reached, the "discharge" phase starts: Surface energy is released, coinciding with a sharp rise in kinetic energy. The surface energy eventually

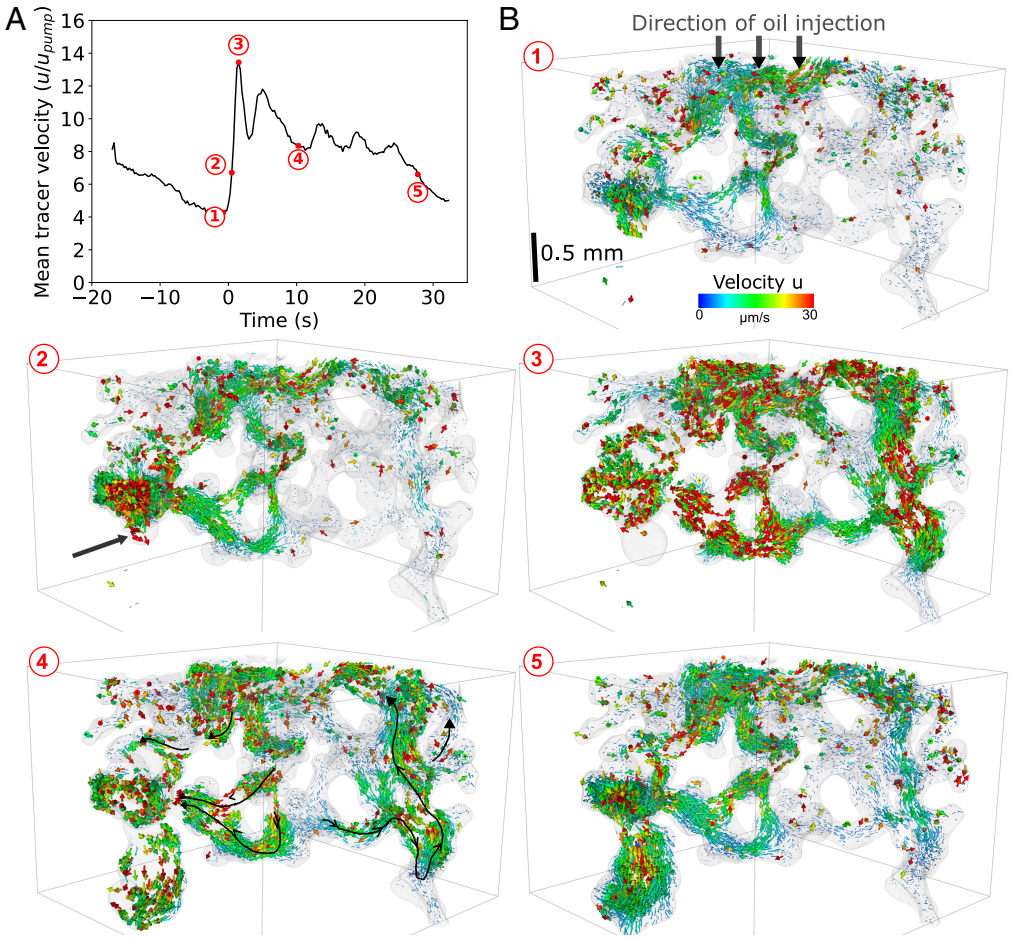

Fig. 2. Particle tracking of flow tracers in the nonwetting phase (oil) during the drainage experiment on the filter sample. (*A*) shows that the flow velocity field peaks at the moment right after the Haines jump depicted in Fig. 1 (indicated with the arrow at time step 2 here). (*B*) 3D renderings at five selected time steps show that this acceleration takes place throughout nearly the entire oil cluster in the sample. After the Haines jump, internal fluid redistribution is performed through remarkably tortuous flow paths which include flow reversal in part of the sample (upward oriented flow paths indicated on rendering 4). A corresponding video can be found in *SI Appendix* (Movie S1, accessible via Figshare: https://figshare.com/s/9b7ee99333c20c83ca01).

decreases to 33% of its peak value. This represents the efficiency with which external work is stored in the menisci over the course of this single Haines jump. This can be compared to estimates of the efficiency in sandstone being around 36% overall (61), noting the granular geometry of our sample. Note that the contact angle used in the calculation has an important impact on this efficiency: The latter decreases for smaller contact angles (i.e., stronger capillary forces). The released surface energy contribution allows the Haines jump to proceed faster than the injection rate delivered by the pump. It decreases in a step-like manner as the meniscus passes through several pores, representing "bumps" in the energy landscape formed by the permissible meniscus locations. This causes secondary acceleration when the meniscus moves through subsequent constrictions. The kinetic energy, in turn, appears to be dissipated mostly as heat (no other contributions match the same trend, except to a minor extent the PV-work). The combined effect with the step-wise "injections" of surface energy results in kinetic energy fluctuations.

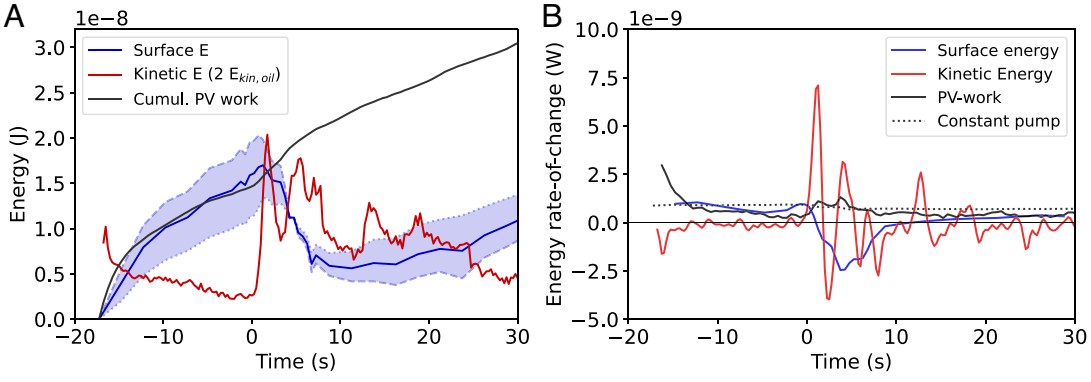

Fig. 3. The energy dynamics of a Haines jump in the porous filter sample. (*A*) The cumulative pressure–volume work, the kinetic energy, and the surface energy determined from the 3D images for the fluid displacement in Fig. 1. The blue shaded area shows the uncertainty on the surface energy when varying the contact angle by ±10°, between 25° and 45°. (*B*) The rate-of-change of the energy contributions, where time zero (by definition) marks the start of the Haines jump.

Finally, approximately 10 s after the Haines jump, a new phase is started when the surface energy starts to be charged again at approximately the same rate as the PV work. This is expected to proceed until the energy barrier of the next Haines jump can be overcome.

1.3. Flow Field Perturbations Spread through the Porous Medium, Affecting Meniscus Dynamics and Solute/Colloid Transport. The kinetic energy fluctuations observed in Section 1.2 reflect perturbations that spread through the flow field in the porous medium as a wavefront. It is important to understand how this spreading takes place, as it causes nonlocal dynamic effects on the fluid menisci: A fluid meniscus in a pore far away from the Haines jump may "feel" the latter's effect due to changes in the flow and pressure field, potentially impacting the displacement.

In Fig. 4, we show how the averaged velocity of tracer particles changes over time in function of their distance to the Haines jump. Close to the Haines jump, the mean flow velocity exceeds the injection rate by a factor 44 in the glass filter sample. *SI Appendix*, Fig. S4 shows that this is a factor 5 for the Ketton limestone sample. Note that the velocity close to the Haines jump may exceed the maximum tracer velocity that we can detect (approximately 4 voxels/scan meaning 44 μm/s), which may result in an underestimation (52). Tracers that are originally positioned further from the Haines jump also undergo acceleration but with a small time delay that increases with the distance to the Haines jump. This delay represents the time for the acceleration in the flow to spread through the porous medium. Our data show that the disturbance to the flow field spreads in the porous medium with a speed of the order mm/s. This is contrary to the pressure fluctuation originating at the Haines jump, which travels at the speed of sound in liquid, on the order of 10^3 m/s in oil. Since inertia is negligible (Reynolds numbers reach maximum 10^{-4}) and the fluid can be treated as incompressible at the observed pressure fluctuations, this indicates that the viscous mass flow limits the propagation of the velocity field fluctuation here. When the pressure wave reaches a certain meniscus, it takes a finite time for the mass flow associated with the local meniscus retraction to take place. This relates the flow dynamics in the bulk to the contact line dynamics (62), which depend on pore wall roughness and viscosity. Our results thus indicate the importance of accurately capturing the effective contact line dynamics in pore-scale simulations.

The fact that the local flow velocities during multiphase flow can be many times higher than the injection flow rate can impact the balance of capillary, viscous, and inertial forces in the pores. It is therefore interesting to characterize the zone of influence of the Haines jump's perturbation to the flow field. Therefore, we investigate the distance over which the velocity fluctuation decays, in units of the samples' characteristic pore sizes. Fig. 4 shows the maximum amplitude of the velocity wave in function of the distance traveled from the Haines jump (i.e., the height of the peaks just after time 0 s in Fig. 4*B*). Viscous liquids undergo damping, suggesting an exponential decay. An exponential fit shows that the characteristic dissipation length is approximately 15 pore lengths for the filter sample and 22 pore lengths for the Ketton limestone sample (*SI Appendix*, Fig. S4).

2. Discussion

The unique 4D velocimetry approach introduced here enables experimental observations of flow field dynamics when one fluid displaces another in a 3D porous material. We apply this to a glass filter and a limestone sample. Our results align well with long-standing observations and simulations of meniscus dynamics during drainage (26, 29, 63, 64) and show that these dynamics drive transient flows in the bulk fluid behind the invading meniscus. These transient flows are an important driver for the complexity of multiphase flow in porous media, which has spurred a decade of research since the first dynamic micro-CT imaging of Haines jumps by Berg et al. (16).

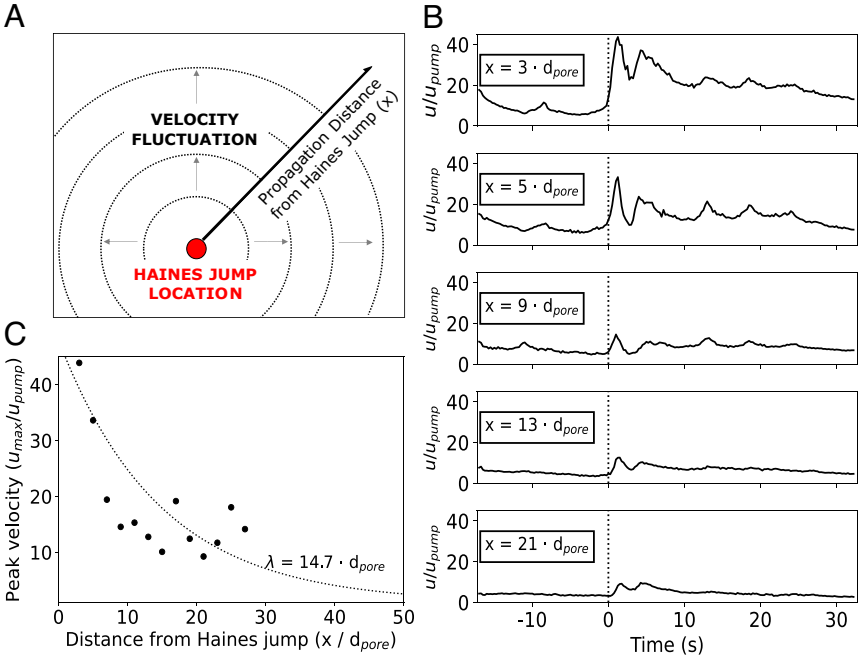

Fig. 4. The Haines jump at time zero is the source of a fluctuation in the velocity field, which propagates through the sample. (*A*) Schematic of the fluctuation propagation. (*B*) Mean local velocity over time for tracer detections at different straight-line distances from the Haines jump location (x), the latter expressed in relation to the sample's mean pore size (d_{pore}). The velocity peak shifts in time for increasing distance, related to the finite propagation speed of the fluctuation. (*C*) The local maximum velocity (velocity peaks in *B*) decays in function of the distance to the Haines jump due to viscous dissipation, with a characteristic decay length λ of 14.7 times the characteristic pore size.

The observed transient flows are linked to a known effect: During a Haines jump, the fluid is internally redistributed by retraction from surrounding pores (16). Our experiments reveal that this results in highly tortuous 3D flow patterns with a characteristic length scale up to 22 pore lengths (for Ketton limestone). The length scale is important as transient flows infer viscous and inertial forces in a local zone of influence around the Haines jump. The measurements thus suggest that nonlocal dynamic effects caused by Haines jumps can be remarkably long-ranged in 3D pore geometries, impacting the representative elementary volume even for relatively homogeneous materials. Previous simulations on simple 2D geometries indicated the influence zones to be smaller, around ~4 pore lengths in ref. 65, while micromodel PIV studies did report long-ranged (yet unquantified) perturbances (30, 66). The large spatial extent of the transient flows also highlights the invalidity of the capillary number to characterize the viscous-capillary force balance: It assumes that viscous forces work on the length scale of a single pore (throat), which is clearly not the case. Finally, we perform the first 3D imaging-based evaluation of how the kinetic and interfacial energy vary during the course of a Haines jump. The results are in line with prior studies which indicated that the flow dynamics are driven by conversion of energy stored in fluid menisci to kinetic energy, with an overall efficiency of around 30 to 40% estimated for sandstone (67, 68). The experiments thus yield unique data to validate pore-scale models on complex pore geometries.

Our experiments are performed with a high-viscosity nonwetting phase (200 mPa s) which improves the tracer particles' stability. In systems with lower fluid viscosities, transient flows may be even more salient. There are several reasons for this. First, Haines jumps may proceed approximately 200 times faster in experiments with decane-like fluid viscosities (~1 mPa s), placing them on the time scale of 10^{-2} s and the velocity scale of 10^{-2} m/s, rather than, respectively, seconds and 10^{-4} m/s in our study. These estimates are in line with previous observations on such fluid systems (16, 58). This is because the magnitude of the velocity perturbation is determined by the local pressure gradient divided by a flow resistance factor which scales with fluid viscosity and depends on pore geometry (65). Second, the high viscosity dampens inertial effects tied to transient flow, e.g., meniscus oscillations, while these can play an important role in, e.g., water–air or water–decane flows (27, 69). In our data, the maximum achieved Reynolds number is of order 10^{-4}, in contrast with (up to) order 10^{2} in such studies. Finally, for lower viscosity systems, the characteristic length scale of the flow perturbations may be larger due to reduced viscous dissipation during the internal fluid redistribution. In other words, it is possible that fluid retraction takes place over a more spread-out region if the viscosity is lower. Note that the precise viscosity scaling is not trivial as it likely also depends on contact line dynamics and pore geometry.

The observation of highly unsteady velocity fields puts forth new questions for solute and colloid transport in multiphase systems. The enhanced dispersion in such systems has so far been fully attributed to the increased tortuosity of flow fields in the presence of a second fluid. Our observations confirm this, but also show important temporal perturbations in the flow field. This could play a role in enhancing solute mixing (70), which may be particularly important when a solute leaches from one of the phases into the other causing concentration gradients near fluid menisci. This is highly relevant for groundwater pollution, e.g., chemicals leaching into the groundwater. Velocity perturbations also have important consequences for colloid remobilization in unsteady two-phase flows, for example, in soil after rain fall. Here, current studies have focused on remobilization when a meniscus passes over an attached colloid, "sweeping" it back into a mobile state. Our results show that unswept particles may still be remobilized by flow field perturbations. Studies in single-phase flow show that remobilization may happen at ~100 μm/s (71), which is well within the range of the velocity peaks expected in water–air systems.

The work presented here opens up the experimental study of the dynamics of flow fields during complex flows in 3D geometries. Nevertheless, further work is needed to extend the findings to a broader range of experimental fluid and flow conditions and a wider range of samples. Furthermore, our observations on multiphase flow dynamics are currently limited to very few pore-filling events. Hence, we do not yet have statistics on fluid invasion events, which is necessary to scale up the results. To make this further work possible, there is a need for methodological improvements, notably improving the temporal and spatial resolutions to increase the dynamic range of the velocimetry measurements and to enable the use of smaller and lighter tracer particles suspended in lower-viscosity fluids.

3. Materials and Methods

3.1. Experimental Design. The experiments were performed on two cylindrical porous samples of 4 mm diameter and 10 mm length: a sintered glass filter (ROBU P0, Germany) and Ketton limestone. They have mean pore sizes of, respectively, 122 μm and 52 μm and image-based porosities of 27 and 14% (Ketton has additional nm-scale porosity, which does not partake in the invasion process here). The pore size distributions are shown in *SI Appendix*, Fig. S5. The wetting fluid is KI-brine (10% KI by weight), while the nonwetting fluid is silicone oil AR200 (Sigma-Aldrich, Belgium). These liquids have viscosities of, respectively, 1 mPa and 200 mPa and densities of 1,074.75 kg/m^3 and 1,070 kg/m^3 at the experiment temperature of 24 °C (72). The interfacial tension is 30 mN m. Both the glass filter and the Ketton limestone are water-wet relative to oil. Typical literature values for advancing/receding contact angles of oil/water on a flat glass plate are, respectively, 44° and 24° (59, 73). For calcite surfaces, decane/water static contact angle varies between 53° and 81° depending on surface roughness (74). Note that contact angles in porous media are known to be different from those measured on flat surfaces due to pore geometry and roughness effects (59).

Silver-coated hollow glass tracer particles with a mean particle size of 10 μm (CoSpheric, USA) were added to the silicone oil (12 mg per g of liquid). The tracer particle size distribution measured by laser diffraction (Malvern Mastersizer 2000) can be found in *SI Appendix*, Fig. S6. The true particle density of 1,080 kg/m^3 is sufficiently close to the silicone oil to avoid effects caused by particle settling and centrifugal forces during the image acquisition. This is proven by negligibly small particle Stokes numbers and terminal velocities due to gravity and centrifugal forces (*SI Appendix*, Texts S3 and S4). Particles were dispersed with an ultrasonic homogenizer (Hielscher UP50H, Germany) and fluids were deaerated by vacuuming while placed in an ultrasonic bath (Bandelin Sonorex TK52, Germany).

The porous samples are inserted in a Viton sleeve mounted in a Hassler-type flow cell made of PEEK, with two flow ports connected to the bottom sample face and one flow port connected to its top face. This flow cell is mounted on the rotation stage of the TOMCAT beam line of the Swiss Light Source (Paul Scherrer Institute, Switzerland), together with two compact high-precision syringe pumps (Harvard Apparatus, USA) which are powered and controlled through electronic slip rings (*SI Appendix*, Fig. S7). Since all flow lines and electrical cables are contained within the rotating setup, the sample can be rotated indefinitely during tomography acquisition, which enables fast and continuous imaging without time gaps. The setup allows us to supply fluids at precisely controlled flow rates during tomography acquisition, down to a minimum set rate of 3.7 nL/min.

At the start of the experiments, the samples are first saturated with deaerated brine at a high flow rate of 25 mL/min, displacing air out of the pores in the sample. The brine is then pressurized to 2 MPa, which is kept as a constant back pressure during the experiment, avoiding difficulties with bubble formation due to the high X-ray flux (56). Next, the silicone oil with tracer particles is injected from the bottom of the sample at 174 nL/min for the filter experiment and 250 nL/min for the limestone experiment. This constant rate corresponds to an estimated

interstitial flow rate in the pores of, respectively, 0.82 μm/s and 2.38 μm/s, resulting in capillary numbers of 5.5×10^{-6} and 1.6×10^{-5}. We start acquiring bursts of tomograms when the oil is first observed on radiographs at the bottom of the sample. The presented results are based on selected bursts where displacements are observed: one where the field-of-view is in the inlet area of the filter sample meaning all the oil in the sample is in the field of view, and one where the field-of-view is further above the inlet area in the Ketton.

3.2. Imaging. The X-ray micro-CT imaging in this work is performed at the TOMCAT beamline, using the GigaFRoST high-speed camera and 4× magnification optics (Optique Peter) (75, 76), resulting in an isotropic voxel size of 2.75 μm and a maximum field of view of 5.5 × 5.5 mm^2. The experiments are performed with a filtered white beam (5 mm glassy carbon and 4 mm borosilicate glass). For each sample, we first acquire dry and brine-saturated reference scans. Then, during the drainage, bursts of 100 or 200 3D images (tomograms) are acquired back-to-back by continuously rotating the sample around its axis. Each tomogram comprises an 180° rotation of the sample, during which 500 or 1,000 radiographs are acquired with an exposure time of 0.5 ms each. This results in a scan time per 3D image of 0.25 s (filter sample) and 0.5 s (Ketton). After acquisition, each time step in the burst (consisting of 500 or 1,000 radiographs) is reconstructed into one 3D image using the gridrec algorithm (77). This was performed twice: once with a Paganin phase retrieval algorithm (78) to maximize contrast between oil and brine and once without it to maximize contrast between tracer particles and oil. Representative example images are shown in *SI Appendix*, Figs. S8–S11 and Movie S2.

3.3. Individual Particle Tracking. The sets of drainage images without phase retrieval were used for individual (Lagrangian) particle tracking using the open-source software package TrackPy (79), based on the methodology described in our earlier work on single-phase flow (52). Further details are available in the supplementary materials (*SI Appendix*, Text S1 and Fig. S12). This yielded approximately 20,000 velocity points per time step in the filter experiment, and 16,000 in the Ketton experiment. Uncertainty quantification of the particle tracking approach for a steady flow indicated that particles with velocities up to 4 voxels/scan can be reliably tracked with velocity errors below 10% (52). In the experiments presented here, 99% of detected velocities are lower than 4 voxels/scan. The maximum local velocity of the fluid meniscus movement (based on local distance between subsequent surface extractions, not on particle tracking) during the Haines jump in the filter sample was approximately 15 voxels/scan. Particle tracers in regions close to such an ongoing Haines jump likely reach a similar maximum velocity and therefore go temporarily undetected due to motion-blurring artifacts. This may result in an underestimation of the mean velocities right after the Haines jump onset. Further validation studies are necessary to fully quantify the measurement uncertainty.

3.4. Image Analysis and Calculation of Energy and Velocity Parameters. The fluid distributions during the experiments are investigated using the set of images reconstructed with phase retrieval. The brine-saturated scan was first registered and subtracted from each drainage time step image. The resulting images have a high contrast-to-noise ratio for brine and oil, and their segmentation is therefore performed with a straightforward automatic Otsu thresholding. These steps are performed using Python/SciPy. The segmented images are post-processed using the despeckle filter in Avizo to remove small noise spots. The result is illustrated in *SI Appendix*, Fig. S13. From this, fluid saturation is calculated at each time step, and the difference image between subsequent time steps yields the rate at which oil retracts (Fig. 1*C*). For the filter sample experiment, the surface areas and mean curvatures of fluid–fluid and fluid–solid interfaces are calculated using the open-source code developed by Khanamiri et al. (80); after downsampling by a factor two to reduce the computational requirements. From this, the energy contributions in Fig. 3 are calculated using the equations in *SI Appendix*, Text S2.

Data, Materials, and Software Availability. Tomography dataset data have been deposited in PSI Public Data Repository (https://doi.org/10.16907/c0dfa6c8-25da-454e-82fa-fc5db7f7c6f2) (81). The code used to analyze the images and the resulting derived data (particle tracks with velocity information, surface properties, and energy calculations) will be made available on https://github.ugent.be/UGCT/XParticleTracking (82).

ACKNOWLEDGMENTS. Dr. Steffen Berg is acknowledged for helpful discussions on Haines jump dynamics. T.B. acknowledges funding from the European Union (ERC Starting Grant, FLOWSCOPY, 101116228) and from the Research Foundation–Flanders (FWO, senior research fellowship 12X0922N). S.E. is a PhD Fellow with the FWO and acknowledges its support under grant 1182822N. We acknowledge partial funding from FWO under research projects G004820N and 3G036518. W.G. and N.M.G. are supported by the Ghent University Special Research Fund (BOFGOA20170007 and BOF.24Y.2018.0007.02, respectively). We acknowledge the Paul Scherrer Institut, Villigen, Switzerland for provision of synchrotron radiation beamtime at the TOMCAT beamline X02DA of the SLS (beam time proposal 20212066).

Author affiliations: [a]Ghent University Centre for X-ray Tomography (UGCT), Ghent University, Ghent 9000, Belgium; [b]Department of Geology, Ghent University, Ghent 9000, Belgium; [c]Swiss Light Source, Paul Scherrer Institute, Villigen PSI 5232, Switzerland; [d]Department of Physics and Astronomy, Ghent University, Ghent 9000, Belgium; and [e]Department of Earth Sciences, Utrecht University, CB Utrecht 3584, The Netherlands

1. M. J. Blunt, *Multiphase Flow in Permeable Media: A Pore-Scale Perspective* (Cambridge University Press, 2017).
2. R. T. Armstrong *et al.*, Beyond Darcy's law: The role of phase topology and ganglion dynamics for two-fluid flow. *Phys. Rev. E* **94**, 043113 (2016).
3. S. Bottero, S. M. Hassanizadeh, P. J. Kleingeld, T. J. Heimovaara, Nonequilibrium capillarity effects in two-phase flow through porous media at different scales. *Water Resour. Res.* **47**, W10505 (2011).
4. A. Rodríguez de Castro, N. Shokri, N. Karadimitriou, M. Oostrom, V. Joekar-Niasar, Experimental study on nonmonotonicity of Capillary Desaturation Curves in a 2-D pore network. *Water Resour. Res.* **51**, 8517–8528 (2015).
5. S. Sinha *et al.*, Effective rheology of two-phase flow in three-dimensional porous media: Experiment and simulation. *Transp. Porous Media* **119**, 77–94 (2017).
6. Y. Zhang, B. Bijeljic, Y. Gao, Q. Lin, M. J. Blunt, Quantification of nonlinear multiphase flow in porous media. *Geophys. Res. Lett.* **48**, e2020GL090477 (2021).
7. Y. Gao, Q. Lin, B. Bijeljic, M. J. Blunt, Pore-scale dynamics and the multiphase Darcy law. *Phys. Rev. Fluids* **5**, 013801 (2020).
8. K. T. Tallakstad *et al.*, Steady-state, simultaneous two-phase flow in porous media: An experimental study. *Phys. Rev. E* **80**, 036308 (2009).
9. M. Rücker *et al.*, From connected pathway flow to ganglion dynamics. *Geophys. Res. Lett.* **42**, 3888–3894 (2015).
10. D. Wildenschild, J. W. W. Hopmans, J. Simunek, Flow rate dependence of soil hydraulic characteristics. *Soil Sci. Soc. Am. J.* **65**, 35 (2001).
11. A. L. Herring, L. Andersson, D. L. L. Newell, J. W. W. Carey, D. Wildenschild, Pore-scale observations of supercritical CO2 drainage in Bentheimer sandstone by synchrotron x-ray imaging. *Intern. J. Greenhouse Gas Control* **25**, 93–101 (2014).
12. S. Schlüter *et al.*, Pore-scale displacement mechanisms as a source of hysteresis for two-phase flow in porous media. *Water Resour Res.* **52**, 2194–2205 (2016).
13. S. Hasan *et al.*, Direct characterization of solute transport in unsaturated porous media using fast X-ray synchrotron microtomography. *Proc. Natl. Acad. Sci. U.S.A.* **117**, 23443–23449 (2020).
14. J. E. Saiers, J. J. Lenhart, Colloid mobilization and transport within unsaturated porous media under transient-flow conditions. *Water Resour Res.* **39**, 1019 (2003).
15. K. J. Dobson *et al.*, 4-D imaging of sub-second dynamics in pore-scale processes using real-time synchrotron X-ray tomography. *Solid Earth* **7**, 1059–1073 (2016).
16. S. Berg *et al.*, Real-time 3D imaging of Haines jumps in porous media flow. *Proc. Natl. Acad. Sci. U.S.A.* **110**, 3755–3759 (2013).
17. M. Andrew, H. Menke, M. J. Blunt, B. Bijeljic, The imaging of dynamic multiphase fluid flow using synchrotron-based X-ray microtomography at reservoir conditions. *Transp. Porous Media* **110**, 1–24 (2015).
18. P. W. Rasmussen, H. O. Sørensen, S. Bruns, A. B. Dahl, A. N. Christensen, Improved dynamic imaging of multiphase flow by constrained tomographic reconstruction. *Sci. Rep.* **11**, 12501 (2021).
19. C. Spurin, T. Bultreys, B. Bijeljic, M. J. Blunt, S. Krevor, Intermittent fluid connectivity during two-phase flow in a heterogeneous carbonate rock. *Phys. Rev. E* **100**, 043103 (2019).
20. C. A. Reynolds, H. Menke, M. Andrew, M. J. Blunt, S. Krevor, Dynamic fluid connectivity during steady-state multiphase flow in a sandstone. *Proc. Natl. Acad. Sci. U.S.A.* **114**, 8187–8192 (2017).
21. A. C. Payatakes, M. M. Dias, Immiscible microdisplacement and ganglion dynamics in porous media. *Rev. Chem. Eng.* **2**, 85–174 (1984).
22. K. Singh *et al.*, Dynamics of snap-off and pore-filling events during two-phase fluid flow in permeable media. *Sci. Rep.* **7**, 5192 (2017).
23. T. Pak, I. B. Butler, S. Geiger, M. I. J. van Dijke, K. S. Sorbie, Droplet fragmentation: 3D imaging of a previously unidentified pore-scale process during multiphase flow in porous media. *Proc. Natl. Acad. Sci. U.S.A.* **112**, 1947–1952 (2015).
24. T. Bultreys *et al.*, Real-time visualization of Haines jumps in sandstone with laboratory-based microcomputed tomography. *Water Resour. Res.* **51**, 8668–8676 (2015).
25. R. Lenormand, E. Touboul, C. Zarcone, Numerical models and experiments on immiscible displacements in porous media. *J. Fluid Mech.* **189**, 165–187 (1988).
26. K. J. Måloy, L. Furuberg, J. Feder, T. Jossang, Dynamics of slow drainage in porous media. *Phys. Rev. Lett.* **68**, 2161–2164 (1992).
27. F. Moebius, D. Or, Pore scale dynamics underlying the motion of drainage fronts in porous media. *Water Resour. Res.* **50**, 8441–8457 (2014).
28. A. L. Herring *et al.*, Observations of nonwetting phase snap-off during drainage. *Adv. Water Resour.* **121**, 32–43 (2018), 10.1016/j.advwatres.2018.07.016.

29. R. T. Armstrong, S. Berg, Interfacial velocities and capillary pressure gradients during Haines jumps. *Phys. Rev. E* **88**, 43010 (2013).
30. S. Roman, C. Soulaine, M. A. AlSaud, A. Kovscek, H. Tchelepi, Particle velocimetry analysis of immiscible two-phase flow in micromodels. *Adv. Water Resour.* **95**, 1–13 (2015).
31. J. E. McClure, S. Berg, R. T. Armstrong, Capillary fluctuations and energy dynamics for flow in porous media. *Phys. Fluids* **33**, 083323 (2021).
32. A. Hansen, E. G. Flekkøy, S. Sinha, P. A. Slotte, A statistical mechanics framework for immiscible and incompressible two-phase flow in porous media. *Adv. Water Resour.* **171**, 104336 (2023).
33. C. Wang, R. Wang, Z. Huo, E. Xie, H. E. Dahlke, Colloid transport through soil and other porous media under transient flow conditions–A review. *WIREs Water* **7**, e1439 (2020).
34. N. K. Karadimitriou, S. M. Hassanizadeh, A review of micromodels and their use in two-phase flow studies. *Vadose Zone J.* **11**, vzj2011.0072 (2012).
35. A. Anbari *et al.*, Microfluidic model porous media: Fabrication and applications. *Small* **14**, 1703575 (2018).
36. A. Jahanbakhsh, K. L. Wlodarczyk, D. P. Hand, R. R. J. Maier, M. M. Maroto-Valer, Review of microfluidic devices and imaging techniques for fluid flow study in porous geomaterials. *Sensors* **20**, 4030 (2020).
37. M. Holzner, V. L. Morales, M. Willmann, M. Dentz, Intermittent Lagrangian velocities and accelerations in three-dimensional porous medium flow. *Phys. Rev. E* **92**, 013015 (2015).
38. S. S. Datta, H. Chiang, T. S. Ramakrishnan, D. A. Weitz, Spatial fluctuations of fluid velocities in flow through a three-dimensional porous medium. *Phys. Rev. Lett.* **111**, 1–5 (2013).
39. S. Franchini, A. Charogiannis, C. N. Markides, M. J. Blunt, S. Krevor, Advances in Water Resources Calibration of astigmatic particle tracking velocimetry based on generalized Gaussian feature extraction. *Adv. Water Resour.* **124**, 1–8 (2019).
40. X. Lu, Y. Zhao, D. J. C. Dennis, Flow measurements in microporous media using micro-particle image velocimetry. *Phys. Rev. Fluids* **3**, 104202 (2018).
41. A. Mascini *et al.*, Fluid invasion dynamics in porous media with complex wettability and connectivity. *Geophys Res. Lett.* **48**, e2021GL095185 (2021).
42. B. Bijeljic, P. Mostaghimi, M. J. Blunt, Insights into non-Fickian solute transport in carbonates. *Water Resour. Res.* **49**, 2714–2728 (2013).
43. M. J. Blunt, *Multiphase Flow in Permeable Media* (Cambridge University Press, 2016), 10.1017/9781316145098.
44. C. Poelma, Ultrasound imaging velocimetry: A review. *Exp. Fluids* **58**, 3 (2017).
45. K. Karlsons *et al.*, Characterizing pore-scale structure-flow correlations in sedimentary rocks using magnetic resonance imaging. *Phys. Rev. E* **103**, 023104 (2021).
46. S. Dubsky *et al.*, Computed tomographic X-ray velocimetry. *Appl. Phys. Lett.* **96**, 023702 (2010).
47. U. Kertzscher, A. Seeger, K. Affeld, L. Goubergrits, E. Wellnhofer, X-ray based particle tracking velocimetry–a measurement technique for multi-phase flows and flows without optical access. *Flow Meas. Instrum.* **15**, 199–206 (2004).
48. W.-K. Lee, K. Fezzaa, T. Uemura, Three-dimensional X-ray micro-velocimetry. *J. Synchrotron Radiat.* **18**, 302–304 (2011).
49. S.-J. Lee, G.-B. Kim, X-ray particle image velocimetry for measuring quantitative flow information inside opaque objects. *J. Appl. Phys.* **94**, 3620–3623 (2003).
50. A. Aliseda, T. J. Heindel, X-ray flow visualization in multiphase flows. *Annu. Rev. Fluid Mech.* **53**, 543–567 (2021).
51. M. Ge, C. Sun, X. Zhang, O. Coutier-Delgosha, G. Zhang, Synchrotron X-ray based particle image velocimetry to measure multiphase streamflow and densitometry. *Radiation Phys. Chem.* **200**, 110395 (2022).
52. T. Bultreys *et al.*, X-ray tomographic micro-particle velocimetry in porous media *Phys. Fluids* **34**, 042008 (2022).
53. S. A. Mäkiharju, J. Dewanckele, M. Boone, C. Wagner, A. Griesser, Tomographic X-ray particle tracking velocimetry. *Exp. Fluids* **63**, 16 (2022).
54. W. B. Haines, Studies in the physical properties of soil: V. The hysteresis effect in capillary properties, and the modes of moisture distribution associated therewith. *J. Agric. Sci.* **20**, 97–116 (1930).
55. C. Spurin *et al.*, Real-time imaging reveals distinct pore scale dynamics during transient and equilibrium subsurface multiphase flow. *Am. Geophys. Union* (2020), 10.1029/2020WR028287.
56. D. E. Meisenheimer, M. L. Rivers, D. Wildenschild, Optimizing pink-beam fast X-ray microtomography for multiphase flow in 3D porous media. *J. Microsc.* **277**, 100–106 (2020).
57. K. Singh *et al.*, Time-resolved synchrotron X-ray micro-tomography datasets of drainage and imbibition in carbonate rocks. *Sci. Data* **5**, 180265 (2018).
58. M. Moura, K. J. Måløy, E. G. Flekkøy, R. Toussaint, Intermittent dynamics of slow drainage experiments in porous media: Characterization under different boundary conditions. *Front. Phys.* **7**, 217 (2020).
59. K. A. Klise, D. Moriarty, H. Yoon, Z. Karpyn, Automated contact angle estimation for three-dimensional X-ray microtomography data. *Adv. Water Res.* **95**, 152–160 (2016).
60. J. E. McClure, S. Berg, R. T. Armstrong, Capillary fluctuations and energy dynamics for flow in porous media. *Phys. Fluids* **33**, 083323 (2021).
61. S. Seth, N. R. Morrow, Efficiency of the conversion of work of drainage to surface energy for sandstone and carbonate. *SPE Reservoir Eval. Engineering* **10**, 338–347 (2007).
62. P. Sheng, M. Zhou, Immiscible-fluid displacement: Contact-line dynamics and the velocity-dependent capillary pressure. *Phys. Rev A (Coll Park)* **45**, 5694–5708 (1992).
63. D. A. DiCarlo, J. I. G. Cidoncha, C. Hickey, Acoustic measurements of pore-scale displacements. *Geophys. Res. Lett.* **30**, 1901 (2003).
64. H. H. Yuan, B. F. Swanson, Resolving pore-space characteristics by rate-controlled porosimetry. *SPE Formation Eval.* **4**, 17–24 (1989).
65. R. T. Armstrong, N. Evseev, D. Koroteev, S. Berg, Modeling the velocity field during Haines jumps in porous media. *Adv. Water Resour.* **77**, 57–68 (2015).
66. G. Blois, J. M. Barros, K. T. Christensen, A microscopic particle image velocimetry method for studying the dynamics of immiscible liquid–liquid interactions in a porous micromodel. *Microfluid Nanofluidics* **18**, 1391–1406 (2015).
67. C. F. Berg, P. A. Slotte, H. H. Khanamiri, Geometrically derived efficiency of slow immiscible displacement in porous media. *Phys. Rev. E* **102**, 033113 (2020).
68. I. Zacharoudiou, E. S. Boek, J. Crawshaw, Pore-scale modeling of drainage displacement patterns in association with geological sequestration of CO_2. *Water Resour Res.* **56**, e2019WR026332 (2020).
69. I. Zacharoudiou, E. S. Boek, Capillary filling and Haines jump dynamics using free energy Lattice Boltzmann simulations. *Adv. Water Resour.* **92**, 43–56 (2016).
70. S. Vedel, H. Bruus, Transient Taylor–Aris dispersion for time-dependent flows in straight channels. *J. Fluid Mech.* **691**, 95–122 (2012).
71. N. Bizmark, J. Schneider, R. D. Priestley, S. S. Datta, Multiscale dynamics of colloidal deposition and erosion in porous media. *Sci. Adv.* **6**, eabc2530 (2020).
72. S. Al Ghafri, G. C. Maitland, J. P. M. Trusler, Densities of aqueous MgCl 2 (aq), CaCl 2 (aq), Kl(aq), NaCl(aq), KCl(aq), AlCl 3 (aq), and (0.964 NaCl + 0.136 KCl)(aq) at temperatures between (283 and 472) K, pressures up to 68.5 MPa, and molalities up to 6 mol·kg^{-1}. *J. Chem. Eng. Data* **57**, 1288–1304 (2012).
73. M. Wei, R. S. Bowman, J. L. Wilson, N. R. Morrow, Wetting properties and stability of silane-treated glass exposed to water, air, and oil. *J. Colloid Interface Sci.* **157**, 154–159 (1993).
74. W. Alnoush, A. Sayed, T. I. Solling, N. Alyafei, Impact of calcite surface roughness in wettability assessment: Interferometry and atomic force microscopy analysis. *J. Pet Sci. Eng.* **203**, 108679 (2021).
75. M. Bührer *et al.*, High-numerical-aperture macroscope optics for time-resolved experiments. *J. Synchrotron Radiat.* **26**, 1161–1172 (2019).
76. R. Mokso *et al.*, GigaFRoST: The gigabit fast readout system for tomography. *J Synchrotron Radiat.* **24**, 1250–1259 (2017).
77. F. Marone, M. Stampanoni, Regridding reconstruction algorithm for real-time tomographic imaging. *J. Synchrotron Radiat.* **19**, 1029–1037 (2012).
78. D. Paganin, T. E. Gureyev, K. M. Pavlov, R. A. Lewis, M. Kitchen, Phase retrieval using coherent imaging systems with linear transfer functions. *Opt. Commun.* **234**, 87–105 (2004).
79. C. Van Der Wel, D. Allan, N. Keim, T. A. Caswell, Trackpy: Fast, Flexible Particle-Tracking Toolkit (2022). https://zenodo.org/records/4682814. Accessed 13 October 2021.
80. H. H. Khanamiri, P. A. Slotte, C. F. Berg, Contact angles in two-phase flow images. *Transp. Porous Media* **135**, 535–553 (2020).
81. T. Bultreys *et al.*, "4D X-ray micro-velocimetry data of multiphase flow perturbations in porous media". PSI. https://doi.psi.ch/detail/10.16907/c0dfa6c8-25da-454e-82fa-fc5db7f7c6f2. Deposited 31 December 2023.
82. T. Bultreys, XParticleTracking: 4D X-ray particle tracking scripts based on TrackPy. Github. https://github.ugent.be/UGCT/XParticleTracking. Deposited 23 February 2024.